Competition between Exceptionally Long-Range Alkyl Sidechain Ordering and Backbone Ordering in Semiconducting Polymers and Its Impact on Electronic and Optoelectronic Properties

Joshua H. Carpenter, Masoud Ghasemi, Eliot Gann, Indunil Angunawela, Samuel J. Stuard, Jeromy James Rech, Earl Ritchie, Brendan T. O'Connor, Joanna Atkin, Wei You, Dean M. DeLongchamp, and Harald Ade*

Intra- and intermolecular ordering greatly impacts the electronic and optoelectronic properties of semiconducting polymers. The interrelationship between ordering of alkyl sidechains and conjugated backbones has yet to be fully detailed, despite much prior effort. Here, the discovery of a highly ordered alkyl sidechain phase in six representative semiconducting polymers, determined from distinct spectroscopic and diffraction signatures, is reported. The sidechain ordering exhibits unusually large coherence lengths (≥70 nm), induces torsional/twisting backbone disorder, and results in a vertically multilayered nanostructure with ordered sidechain layers alternating with disordered backbone layers. Calorimetry and in situ variable temperature scattering measurements in a model system poly{4-(5-(4,8-bis(3-butylnonyl)-6-methylbenzo[1,2-b:4,5-b′]dithiophen-2-yl)thiophen-2-yl)-2-(2-butyloctyl)-5,6-difluoro-7-(5-methylthiophen-2-yl)-2H-benzo[d][1,2,3]triazole} (PBnDT-FTAZ) clearly delineate this competition of ordering that prevents simultaneous long-range order of both moieties. The long-range sidechain ordering can be exploited as a transient state to fabricate PBnDT-FTAZ films with an atypical edge-on texture and 2.5× improved field-effect transistor mobility. The observed influence of ordering between the moieties implies that improved molecular design can produce synergistic rather than destructive ordering effects. Given the large sidechain coherence lengths observed, such synergistic ordering should greatly improve the coherence length of backbone ordering and thereby improve electronic and optoelectronic properties such as charge transport and exciton diffusion lengths.

1. Introduction

The two dissimilar constituents of semiconducting polymers (SCPs), the semiconducting conjugated backbone and insulating alkyl sidechains, cause complex and competing phenomena in terms of material phase behavior,[1,2] morphology formation,[3–6] and local ordering,[7–12] that inherently affect material performance. Results in the literature for SCPs that are generally more crystalline and have simpler backbone structures, such as polyakylthiophenes (PATs), demonstrate that ordering in the backbone and π-stacking directions are not necessarily strongly correlated with ordering in the alkyl stacking direction or ordering between alkyl sidechains, especially in materials having sufficiently high molecular weight.[13,14] More broadly, it has been shown that phase separation between backbone and alkyl sidechain is a rather general trait among SCPs and that ordering within the alkyl nanodomains can occur even when the nanodomains of the more rigid backbones are amorphous, e.g., in regiorandom PATs.[15,16] Whether sidechains can readily order independently of the aromatic backbones and form separate nanophases when monomer structures and sidechain attachments are highly asymmetric, as is often the case for amorphous donor–acceptor (D–A) copolymers, is currently an open question.

Studies of ordering in SCPs have shown correlations between backbone ordering and both charge transport and spectroscopic

Dr. J. H. Carpenter, Dr. M. Ghasemi, I. Angunawela, S. J. Stuard, Prof. H. Ade
Department of Physics and Organic and Carbon Electronics Lab (ORaCEL)
North Carolina State University
Raleigh, NC 27695, USA
E-mail: harald_ade@ncsu.edu

Dr. E. Gann, Dr. D. M. DeLongchamp
Materials Science and Engineering Division
National Institute of Standards and Technology
100 Bureau Drive, Gaithersburg, MD 20899, USA

J. J. Rech, E. Ritchie, Prof. J. Atkin, Prof. W. You
Department of Chemistry
University of North Carolina at Chapel Hill
Chapel Hill, NC 27599-3290, USA

Prof. B. T. O'Connor
Department of Mechanical and Aerospace Engineering and ORaCEL
North Carolina State University
Raleigh, NC 27695, USA

signatures, reflecting aggregation or exciton bandwidth.[13,17–24] In broad qualitative agreement with results from inorganic and organic small molecule semiconductors, much of the early work has shown strong correlations between crystalline order and high charge carrier mobility.[21,25–27] However, for many more recently synthesized SCPs, including many D–A-type copolymers with stiffer backbones, it has been shown that an overall high degree of crystallinity or large crystalline coherence length is not necessary for good charge transport;[13,28,29] instead, the key morphological parameters are torsional backbone order, short range intermolecular order (i.e., aggregation or paracrystalline order), and sufficiently high molecular weight (≥50 monomer units). Regarding the first factor, the torsional disorder of the backbone, we note that sexithiophene molecules are highly planar within crystals,[30,31] yet in nominal P3HT crystals, backbones are nonplanar with significant distributions of dihedral angles between thiophene units.[32–34] Dihedral angles significantly deviating from coplanarity along the backbone, i.e., backbone disorder, highlight the negative impact sidechains can have and by extension imply an imperfect molecular design that constrains backbone planarity. Additionally, for SCPs having sufficiently high molecular weight, Noriega et al. found that the paracrystallinity parameter (g) in the π-stacking direction was ≥6% for a broad cross-section of SCPs.[13] Based on the classifications of SCPs as paracrystalline ($g \approx$ 6–8%) or amorphous ($g \approx$ 10–20%) of Noriega et al., many of the more recently synthesized high mobility D–A copolymers are considered to be largely amorphous. This generally observed high degree of paracrystallinity might reflect the competing ordering between sidechains and backbones and does not exclude the possibility

of improving these mobilities further by rationally utilizing sidechain order to induce improvements in backbone order.[35] Such synergistic ordering is an avenue of molecular design that is yet to be explored for alkyl sidechains.

In this work, we report the discovery of a highly ordered alkyl sidechain phase with exceptionally long crystalline coherence length that strongly affects SCP backbone order, optical aggregation, and film microstructure. Films with such sidechain ordering are fabricated by drop-casting from low volatility solvents at room temperature (RT), without any subsequent processing. We characterize the highly ordered sidechain phase and the resulting effects on backbone order and film microstructure in detail using poly{4-(5-(4,8-bis(3-butylnonyl)-6-methylbenzo[1,2-b:4,5-b′]dithiophen-2-yl)thiophen-2-yl)-2-(2-butyloctyl)-5,6-difluoro-7-(5-methylthiophen-2-yl)-2H-benzo[d][1,2,3]triazole} (PBnDT-FTAZ) as a model system. FTAZ is an amorphous D–A type SCP with $g \approx$ 15% in π-stacking direction and no differential scanning calorimetry (DSC) melting peak >50 °C for typical spin-casting processing conditions and solvents. We find that the ordered sidechains in our drop-cast films induce significant torsional disorder in the backbone (as observed by spectroscopy), as well as a nanophase composite multilayer consisting of the crystalline insulating sidechain domains and the disordered optoelectronically active backbone domains. Upon melting of the highly ordered sidechain phase, the roughly edge-on backbone configuration remains, yielding in-plane (edge-on) π-stacking. To visualize the differences, **Figure 1**b,c illustrates the inferred nanostructure in the FTAZ film with the highly ordered sidechain phase as well as concomitant detrimental effects on backbone ordering as they compare to the ordering present after melting the sidechains in Figure 1d,e. We exploit the
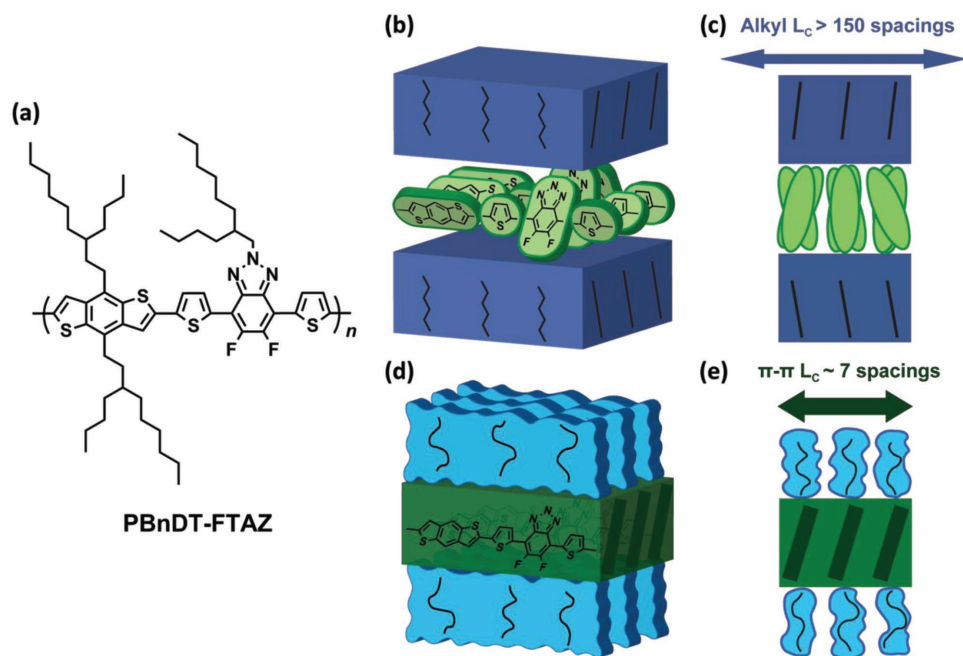

Figure 1. a) Structure of FTAZ. b–e) Conceptualization of the competition in ordering between sidechains and backbones in FTAZ. The long-range 2D crystalline order of the sidechain layers in the drop-cast samples induces torsional disorder in the backbone, preventing intermolecular π-stacking, as shown at an angle in (b) and along the backbone direction in (c). When the highly ordered sidechain phase has melted, the backbones are no longer as torsionally constrained and can π-stack more efficiently, though with a much shorter coherence length than exhibited by the sidechain crystals, as shown at an angle in (d) and along the backbone direction in (e).

sidechain ordering and the induced backbone order after subsequently melting to improve charge mobility in organic field-effect transistors (OFETs) by a factor of 2.5, demonstrating one of many ways this highly ordered sidechain phase could potentially be utilized. We further show that this highly ordered sidechain phase is a general feature of the phase behavior and ordering of a series of SCPs with varying monomer structures, sidechain attachment densities, amounts of sidechain branching, and typical paracrystallinity values. Finally, we hope that our findings can inspire improved material design, where synthetic chemists will utilize this propensity for long-range alkyl sidechain ordering to facilitate similar long-range backbone ordering as a strategy for improving material properties that yields enhanced performance.

2. Results

FTAZ films were drop-cast from relatively low volatility solvents, such as chlorobenzene (CB), and left to dry at RT to achieve a very slow solvent quench that increases the ability of the sample to approach local thermodynamic equilibrium and maximizes the degree of sidechain order (see the Experimental Section for details). Spin-cast samples were also prepared from the same solution for comparison. The samples were investigated with a number of methods, generally investigating first the local bond ordering, then the mesoscopic ordering, and eventually the relationship to thermodynamic transitions.

In order to explore local structural ordering and overall preferred bond orientation at the film surface, we performed near-edge X-ray absorption fine structure (NEXAFS) spectroscopy. Total electron yield (TEY) NEXAFS spectra using p-polarized X-rays at varying angles of incidence are shown for FTAZ films drop-cast and spin-cast from CB in **Figure 2**a,b, respectively, where 90° is normal incidence. From 287 to 290 eV, where C 1s → σ^*_{C-H} resonances appear both for alkanes and SCPs,[36–40] the drop-cast spectra clearly has two peaks at 287.4 and 288.1 eV that are highly dichroic. In neat alkanes this energetic splitting indicates crystallinity because, for all-trans chains, the C 1s → σ^*_{C-H} transitions are orthogonal to the chain axis to either the lowest unoccupied molecular orbital (LUMO) or LUMO+1, of which the probability densities are predominantly in the plane defined by the chain zigzag or normal to it, respectively[40,41] (for a reproduction of previously published data on nonadecane single crystals that completely reflect the essence of the drop data here, see Figure S1 in the Supporting Information). The average transition dipole moment (TDM) of both these transitions together, quantified by a fit to intensity versus incident angle,[36] is oriented 74° from film normal, i.e., highly in-plane. This is in strong contrast to the spin-cast sample, for which there is only a single peak in this region, as is typical for amorphous alkanes,[40] with an average TDM of 57° from normal, very close to the magic angle of 55° which indicates a lack of preferential orientation. These spectral differences signify that, while the sidechains in the spin-cast sample are amorphous with very little orientational order, the sidechains in the drop-cast sample are highly crystalline and highly oriented (for extended discussion of NEXAFS data and fits, see Section S2 in the Supporting Information).
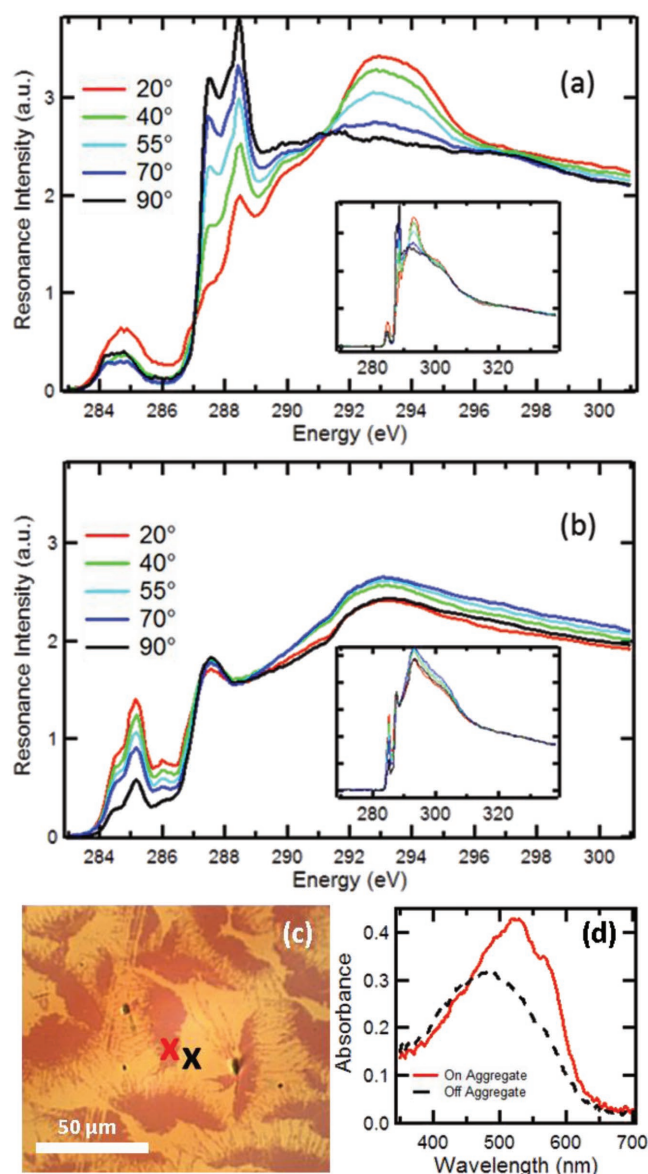

Figure 2. Incident angle dependent TEY NEXAFS spectra of a) drop-cast and b) spin-cast FTAZ using p-polarized X-rays, normalized to 320 eV, where 90° is normal incidence. Insets show full measured energy range. d) Micro-UV–vis spectra of an optically aggregated and nonaggregated region of the drop-cast FTAZ film are shown with c) locations where the spectra were measured shown in a microscopy image.

This analysis is confirmed by the C 1s → σ^*_{C-C} transitions in the 291–296 eV region, with TDMs parallel to the alkyl chain axis direction.[36,37,42] In the drop-cast spectra, there are two distinct peaks in this region which mirror the splitting of the C−H signature due to the high symmetry of the all-trans conformations of the crystalline sidechains.[40,41,43] These transitions are also highly dichroic, with an average TDM 42° from normal, i.e., tilted, but generally out-of-plane. The extracted average TDM directions from this spectral region are not as accurate due to background issues such as uncertainty in the signal from the C−C bonds in the backbone and C 1s to continuum transitions. Nonetheless, the TDMs for C−H and C−C

1806977 (3 of 13)

are confirmed to be essentially orthogonal as they should be. Note that because of both the branching of the sidechains and the lack of a well-known global orientation of the molecules, it is not possible to determine the exact average direction of the sidechains from these spectra. In the spin-cast spectra, there is the typical single C 1s → σ^*_{C-C} transition, with a calculated average TDM of 57.4° from normal, further demonstrating a lack of sidechain orientational order in the control sample.

Below the C 1s ionization potential at ≈290 eV and the C 1s → σ^*_{C-H} transitions, the spin-cast spectra have three clearly observable peaks at 284.5, 285.2, and 286 eV, in agreement with previously published transmission NEXAFS spectra.[44] A fourth peak at 287 eV was necessary to attain a good fit to the spectra that was neither obvious nor noted in previous reports. While detailed assignments of these peaks to specific transitions have not been published for FTAZ, it is well established that materials with thiophene and related aromatic moieties typically have a C 1s → $\pi^*_{C=C}$ peak at ≈285.2 eV.[45] Orbital delocalization is commonly attributed with splitting and shifting π^* transition intensity into multiple peaks,[46] while substitutions of more electronegative heteroatoms are also known to shift transitions to higher energy relative to materials without the substitutions.[47–49] The peaks in the π^* manifold of FTAZ are likely due to a combination of these factors since it has two thiophene units, an FTAZ unit with nitrogen and fluorine heteroatoms, and relatively high charge carrier mobility (and therefore some degree of orbital delocalization between backbone units).

The substantial differences in the C 1s → $\pi^*_{C=C}$ transition region from ≈283.5 to 287 eV between spin-cast and drop-cast NEXAFS spectra as well as micro-UV–vis spectra of the drop-cast film demonstrate that the highly ordered sidechains strongly affect the torsional disorder between backbone units and therefore the electronic coupling of the polymer backbone. In the drop-cast NEXAFS spectra, the intensity of the lowest energy region of the manifold is increased relative to the rest and there is significant broadening of the peaks relative to those in the spin-cast spectra, so that their positions are not as clearly defined. When peaks are fit to the drop-cast spectra and peak positions allowed to vary, the peak positions shift slightly, though the quality of the fits are comparable to those with the energies held constant. The increased intensity at lower energy relative to the rest of the π^* manifold and the substantial overall peak broadening within the manifold of the drop-cast spectra are similar to effects reported in P3HT spectra,[50] which were shown to be due to an increase in the range of torsional angles between neighboring backbone units. This interpretation is supported by the dichroism of the π^* manifolds, which yielded an average TDM 54.2° from normal for the drop-cast film and 46.2° from normal for the spin-cast film. These differences show that there is no preferential orientation of the π^* TDMs in the drop-cast film, while FTAZ in the spin-cast film adopts a more face-on orientation. The micro-UV–vis spectra in Figure 2d (from a drop-cast sample aged at RT for 5 months) provide further evidence of the effect of sidechain crystallinity on electronic coupling. The spectrum measured on an aggregate in the drop-cast film (locations shown in Figure 2c) has a clear aggregate optical signature that corresponds to chromophore, i.e., backbone ordering, whereas elsewhere the absorption is featureless, indicating completely disordered backbones

with little optoelectronic coupling between neighboring chromophores. The coexistence in the drop-cast film of the two phases with disordered/ordered and ordered/disordered sidechains/backbones, respectively, with an area and thus volume fraction of roughly 50:50 implies that the average NEXAFS TDM orientation discussed above is a mixture of amorphous and nearly perfectly oriented alkane sidechains with a TDM orientation of 33° from film normal for the alkyl chain axis. The NEXAFS spectra of the drop-cast sample thus clearly reflect crystalline sidechains and, together with the UV–vis data, demonstrate the resultant effect on backbone torsional ordering.

Grazing incidence wide angle X-ray scattering (GIWAXS) patterns require longer range ordering than spectroscopic methods to produce a signal and were used for spin-cast and drop-cast FTAZ films (**Figure 3**a,b, respectively) to help further elucidate the spatial extent of this sidechain ordering and the effect it has on FTAZ backbones and overall microstructure. The GIWAXS pattern of the drop-cast sample has a series of relatively intense peaks, very narrow in q, beginning in the in-plane direction at $q_{xy} = 1.47$ Å^{-1} and corresponding to a real space distance of 4.27 Å, extending in the q_z direction with a distinct maximum in intensity for the third peak in q_z above $q_{xy} = 1.47$ Å^{-1} (features shown zoomed-in and highlighted with a green arrow in Figure 3f). The 4.27 Å spacing is within 4% of most reports of the spacing between nearest neighbor chains in short chain ($n \leq 16$) n-alkane crystals.[51,52] We also note that the third peak in this series in q_z also appears very weakly in the spin-cast film (see Figure 3a,c), which was not annealed or otherwise treated post casting, meaning that it took some time (albeit a considerably shorter period) to fully dry as well. The separation in q_z between the peaks in this series corresponds to that of the similarly narrow and also previously unobserved peaks in the out-of-plane direction at $q_{xy} = 0$ (features shown zoomed-in and highlighted with pink arrows in Figure 3e), beginning at $q_z = 0.152$ Å^{-1} with at least six diffraction orders visible and measured at exactly $q_{xy} = 0$ with X-ray diffraction (XRD) in θ–2θ geometry (Figure S7, Supporting Information).

The next most significant, if less striking, differences between the scattering patterns from the drop-cast and spin-cast films are between the typical SCP scattering features. There is a noticeable difference in the orientation distribution of the (100) alkyl stacking peak intensity at $q \approx 0.33$ Å^{-1}, seen most clearly in the 1D profiles in Figure 3c. The spin-cast sample has a face-on texture as has been shown previously to be the norm for neat spin-cast FTAZ films,[53] with a corresponding out-of-plane π-stacking peak ($q \approx 1.68$ Å^{-1}). In contrast, the drop-cast sample has significantly more (100) intensity out-of-plane than in-plane, importantly, without a commensurate increase in in-plane π-stacking intensity.

While a full physical description of the exceptional ordering indicated by the scattering pattern of the drop-cast samples will require careful further study and is beyond the scope of this paper, we give a brief description here of our interpretation of both the sidechain ordering and the overall microstructure (for extended GIWAXS discussion see Section S3 in the Supporting Information). The sharp peak in-plane at $q = 1.47$ Å^{-1} in the drop-cast pattern signifies very strong ordering in-plane of nearest neighbor alkyl sidechains, which are between polymers with backbone axis in-plane. Peak widths in q_{xy} correspond to
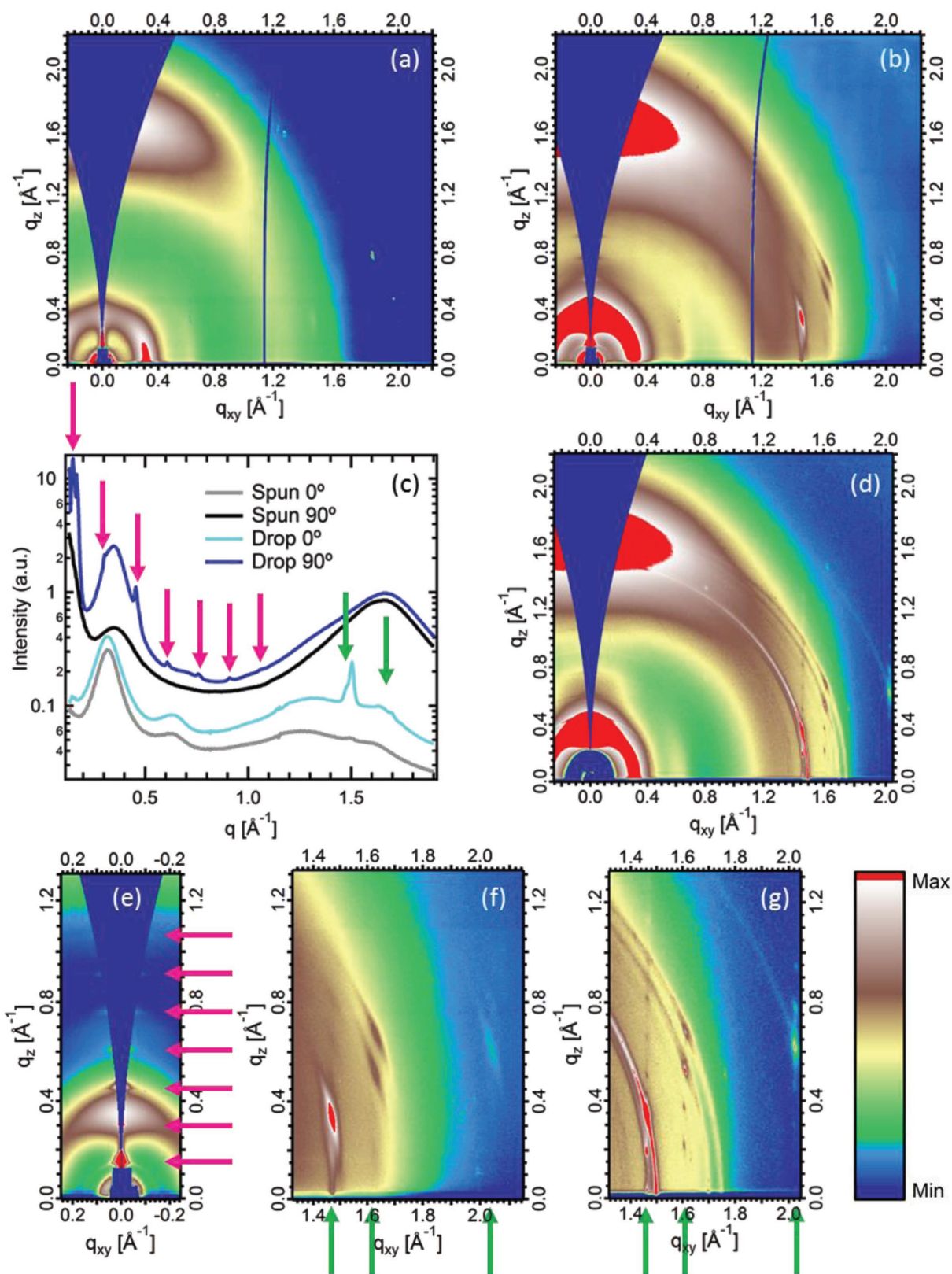
Figure 3. 2D GIWAXS patterns of FTAZ films a) spin-cast and b) drop-cast from CB measured 7 days after film drying. c) In-plane and out-of-plane azimuthally averaged GIWAXS intensity versus q profiles for both are shown. d) 2D GIWAXS pattern of drop-cast FTAZ (measured at a second beamline after 40 days of storage at RT). e) Zoomed-in portion of the out-of-plane low-q region of the scattering pattern in (b), while f) zoomed-in portion of

the experimental resolution of beamline 7.3.3 at the Advanced Light Source (ALS) in Figure 3b,e,f, so measurements were also done at beamline 11-3 at the Stanford Synchrotron Radiation Lightsource (SSRL) (Figure 3d,g, see the Experimental Section for details), where peak widths also corresponded to the experimental resolution and give a lower limit on the coherence length (per single peak Scherrer analysis) in-plane between sidechains of 70 nm (>160 intermolecular spacings), an exceptionally large value for SCP ordering. We note that the drop-cast sample used for Figure 3d,g was also aged for 40 days at RT which we found, along with increasing solvent boiling point (and therefore drying time), to cause changes in the intensity distribution of some of the sidechain features in azimuthal angle χ. This led to an almost isotropically distributed ring in addition to the more intense, highly oriented scattering features. Changes in peak width of these very sharp peaks with aging could not be determined since at both the beamlines, peak widths were limited by the experimental resolution. The changes in the drop-cast scattering patterns with aging at RT were accompanied by observable changes in aggregation with optical microscopy (data not presented here). The exact origin of the spacing indicated out-of-plane in the drop-cast pattern is less clear, as the first order q_z value equates to a real space distance of 4.2 nm. The width in q_z is also the experimental resolution in this direction, giving a lower limit of the coherence length in this direction of >100 nm (>25 spacings). These peaks at $q_{xy} = 0$ closely resemble those reported for a spacing in a P3HT "supercell" configuration over multiple backbones and sidechains, which we note appear when films are treated at low temperatures (and therefore potentially involve sidechain ordering).[54] Our data cannot confirm a "supercell" structure for FTAZ and determining the exact packing indicated by these atypical scattering patterns will require further study, however the large size of the observed out-of-plane spacing implies that it extends across multiple backbones and sidechains. Given that the backbone is disordered in the drop-cast sample as observed by the above spectroscopy data, these out-of-plane peaks do not have a crystallographic unit cell and should be thought of as Bragg diffraction of nanoscale multilayers. This out-of-plane order, along with both the scattering (marked increase in intensity of the typical out-of-plane (100) peak with no accompanying increase in in-plane π-stacking intensity) and spectroscopic evidence for a significant population of disordered backbones in the drop-cast sample, suggests a nanophase separated layered morphology with layers of 2D crystalline alkyl sidechains alternating with torsionally disordered backbone layers that are not able to π-stack in-plane, consistent with the spectroscopy data. The fact that there are several orders of all the alkyl sidechain peaks in the out-of-plane direction suggests that, despite the torsional disorder along the backbone, there is very good registry between alkyl sidechain layers in this direction over multiple typical (h00) spacings, i.e., across multiple phase separations. We note that changes in the more typical SCP scattering features coinciding

with the highly ordered sidechain features appear to be in addition to scattering features similar to those of the spin-cast film, indicating a separate population of face-on FTAZ without sidechain ordering and corroborating the image in Figure 2c that indicates two distinct FTAZ populations.

To further study the complex microstructure and long-range alkyl sidechain ordering of FTAZ and its origins, we correlated temperature dependent in situ GIWAXS with DSC thermograms. The GIWAXS patterns were measured from a film drop-cast from TCB and measured after aging for 3 days at RT (postdrying) at varying temperature from 35 to 200 °C. The pattern at the first temperature step (35 °C) of the in situ measurements, which shows no significant changes to the scattering pattern yet, is shown in **Figure 4**a and is very similar to the pattern of the aged sample drop-cast from CB and shown in Figure 3d (for all in situ patterns, see Section S4 in the Supporting Information). To best visualize and quantify the changes to the sidechain features with temperature, ±2° cake slices about the direction of the maximum intensity sidechain peak (12° from in-plane relative to the beam center) are plotted in Figure 4c,d, to show both the low and high q features, respectively. From peak fits to these 1D profiles, the peak areas of the strongest sidechain peak (≈1.5 Å^{-1}, labeled high q) and the layer spacing peak areas (≈0.15 Å^{-1}, labeled low q) were normalized to their value at 35 °C and plotted in Figure 4e. Both the sets of features show a monotonic and completely simultaneous decrease in relative intensity from 35 to 65 °C and disappear completely at 70 °C. To correlate these diffraction changes to thermodynamic transitions, we overplot the endothermic transitions of samples drop-cast from CB and TCB observed in DSC thermographs and find that the disappearance of the diffraction spots are in excellent agreement with the position of the DSC melting peak for the TCB cast film (indicated by a vertical dashed line in Figure 4e). From these data, a coherent picture emerges of crystalline sidechains that melt at ≈50 °C. In pure alkane crystals, this melting temperature would approximately correspond to that of linear n-tricosane or n-tetracosane (C$_{23}$H$_{48}$ or C$_{24}$H$_{50}$).[55,56] Given that the sidechains are shorter than the equivalent alkane, we note that one end of the sidechains is pinned due to the backbone attachment reducing possible entropic gains. Since even a doubling of the sidechain lengths would be insufficient to reach the observed melting temperature, we speculate that the sidechain melting is accompanied by a change in the backbone packing that has also an endothermic sign.

The scattering data from 70 to 200 °C provide a structural description of this accompanying change in backbone packing. Over this higher temperature range, there is a clear, dramatic increase in the in-plane π-stacking peak intensity relative to the rest of the scattering pattern. This coincides with an increase in intensity and narrowing of three orders of conventional out-of-plane lamellar peaks involving melted or amorphous sidechains. Both the sets of features are shown most clearly in Figure 4b, after the in situ measurements and

the in-plane high-q region of (b). g) The zoomed-in, in-plane high-q portion of (d). In (c), (e), (f), and (g), the green arrows highlight the location of in-plane features in q_{xy} and the pink arrows highlight the location of out-of-plane features in q_z. The log intensity color scale (shown) was scaled for each pattern to make the features most visible. The scale has the same values between (b) and (f), but different between (b) and (e).
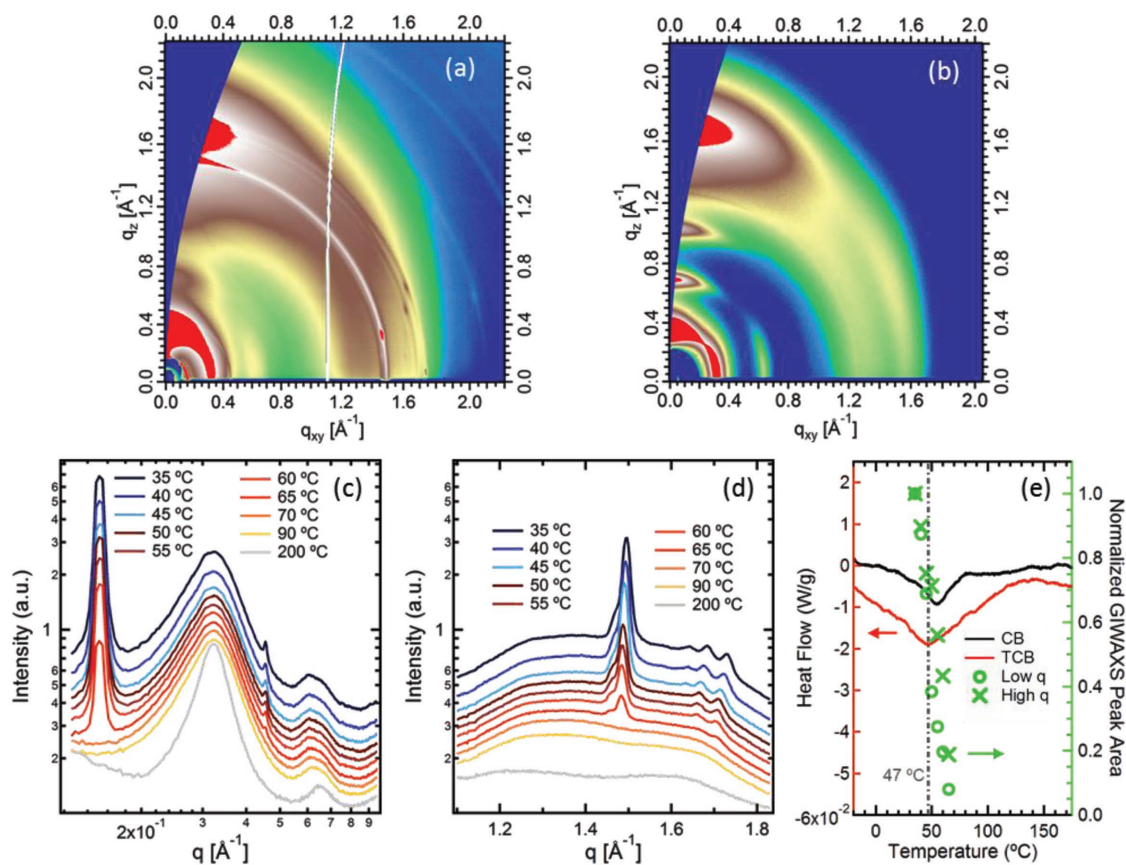
Figure 4. a) 2D GIWAXS pattern of FTAZ drop-cast from TCB at the first temperature step during in situ heating (35 °C). b) 2D GIWAXS pattern of FTAZ drop-cast from TCB and after annealing and cooling to RT. Azimuthally averaged (±2°) GIWAXS intensity versus q profiles in the direction of the most intense sidechain scattering peak (at 1.5 Å^{-1}, 12° from in-plane relative to the beam center) at varying temperature for the FTAZ film drop-cast from TCB are shown at c) low q and d) high q. e) DSC thermograms of FTAZ drop-cast from CB and TCB in the temperature range of the sidechain melting peak, plotted with the normalized sidechain ($q \approx 1.5$ Å^{-1}, labeled high q) and layer spacing ($q \approx 0.15$ Å^{-1}, labeled low q) peak areas at varying temperature as calculated from peak fits to the profiles in (c) and (d). The dashed vertical line at 47 °C indicates the temperature of the DSC melting peak of the TCB cast film.

cooling back to RT, but the changes can also be observed in each scattering pattern in Section S4 (Supporting Information). This comports with our description above of the frustrated backbone packing originally present in the drop-cast samples and illustrated in Figure 1b,c, where the FTAZ backbones with crystalline sidechains are in a roughly edge-on configuration but torsionally disordered such that they are not able to efficiently π-stack until after the sidechains melt. We note that the samples that initially exhibited strong sidechain ordering and were annealed above the melting temperature of the sidechains then cooled to RT represent the strongest conventional SCP backbone ordering achieved for FTAZ. Overall, the temperature-dependent data confirm the interpretation of the NEXAFS and UV–vis results described above that the sidechain and backbone ordering are competing and the highly ordered sidechain phase inhibits π-stacking between neighboring backbones. Additionally, the increased conventional backbone ordering observed after processing via the melting of the highly ordered sidechain phases also suggests a way to utilize the sidechain ordering in FTAZ to create a microstructure that could be more favorable for in-plane charge transport.

Having established the characteristic signatures of this highly ordered sidechain phase and measured its effects, along with those of its subsequent melting, on backbone ordering and film microstructure, we endeavored to exploit this knowledge to improve in-plane charge transport properties in OFETs. Based on the in situ variable temperature GIWAXS data, our hypothesis was that in-plane charge transport could be improved in drop-cast films relative to spin-cast films by using sidechain ordering to induce a relatively edge-on molecular packing, where the ordered sidechain phase could then be melted to ultimately achieve improved in-plane π-stacking. In order to test this hypothesis, derived from early work on P3HT,[21] we fabricated OFETs employing spin-cast and drop-cast films to measure differences in mobility before and after undergoing the same variable temperature treatment as the in situ GIWAXS samples, hereafter referred to as annealing. This required careful choice of device architecture and consideration of the applicability of our GIWAXS results above this configuration.

To compare in-plane charge transport between spin-cast films and drop-cast films, bottom gate bottom contact (BGBC) OFETs were employed, as drop-cast samples are micrometers
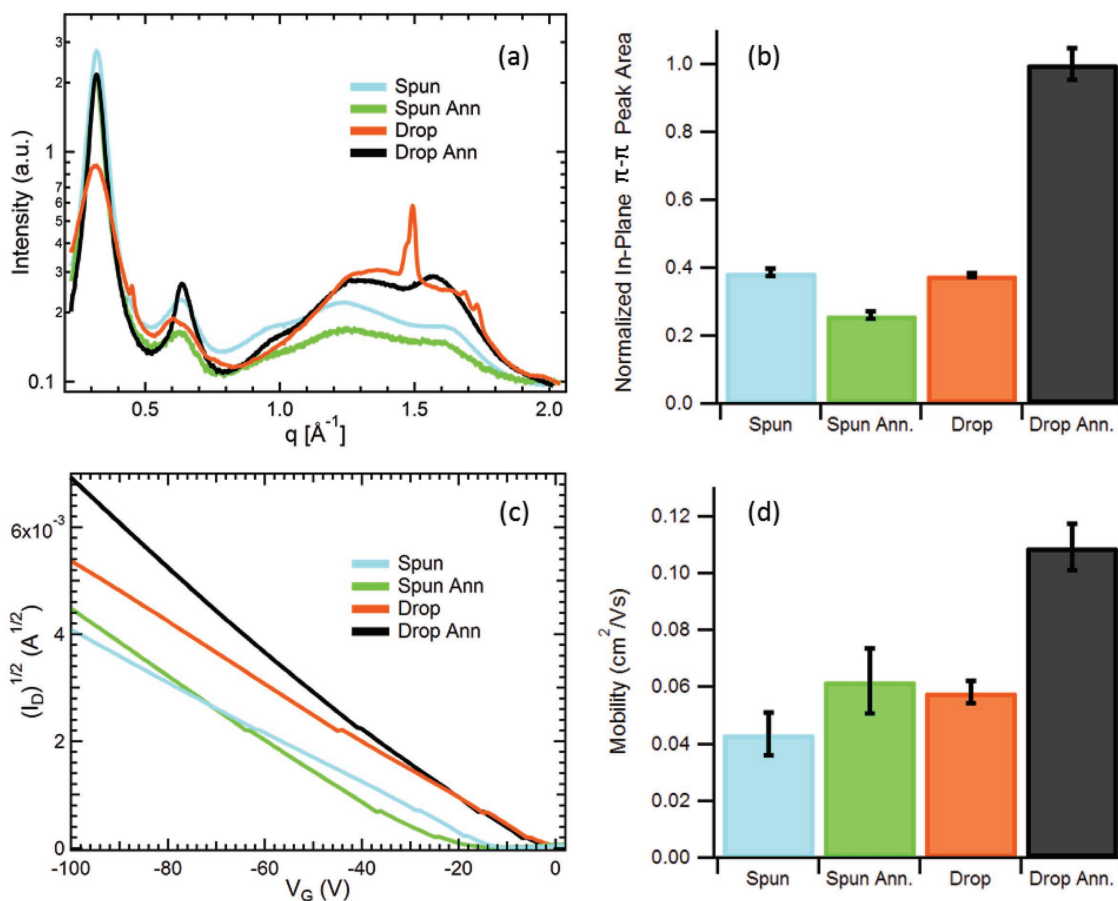
Figure 5. a) In-plane GIWAXS intensity versus q profiles of FTAZ spin-cast and drop-cast from TCB, before and after annealing. b) Normalized area of the in-plane π-stacking peak for each sample as fit to the profiles. c) Typical OFET transfer curves ($V_d = -100$ V) in the saturation regime for the different film preparation conditions. d) Average mobilities of $n > 30$ devices for each condition extracted from transfer curves, with one standard deviation error.

thick with considerable thickness variation and present considerable device engineering difficulties in other geometries. To confirm that the conclusions reached above about molecular packing are valid in the charge transport layer at the interface with the substrate dielectric, we measured GIWAXS patterns, both above and below the critical angle for the surface of a drop-cast film, but also after drop-casting on a water soluble layer, floating the film, flipping it upside down on a blank substrate, and then recording scattering patterns below and above the critical angle for what was originally the lower interface of the film. The full results and discussion are given in Section S6 (Supporting Information) but, in summary, we find that the scattering patterns recorded on the floated and flipped film are effectively identical to that presented in Figure 4a, and therefore we expect the conclusions from the GIWAXS results presented above to hold.

One set of OFETs was prepared employing spin-cast FTAZ films from TCB, as described previously,[53] while another was prepared that employed films drop-cast from TCB, prepared identically to those characterized with TEY NEXAFS, GIWAXS, and DSC above. Device $I-V$ characteristics were measured, then devices were subsequently annealed and measured again. Full device preparation conditions are described in the experimental section and follow those previously reported for FTAZ

OFETs where applicable.[53] At least 30 devices were tested for each preparation condition and average on/off ratios, threshold voltages, and mobilities are reported in Table S6 and Section S8 (Supporting Information) along with an extended discussion of the data. Average mobility values for drop-cast and spin-cast devices before and after annealing along with typical transfer curves from individual devices are shown in **Figure 5**d,c, respectively. While drop-cast devices have marginally higher average mobility than spin-cast devices before annealing (5.8 ± 0.4 vs $4.3 \pm 0.8 \times 10^{-2}$ cm^2 V^{-1} s^{-1}), after annealing, the average mobility of the drop-cast devices improves to $1.1 \pm 0.08 \times 10^{-1}$ cm^2 V^{-1} s^{-1}, while that of the spin-cast devices only improves to $6.2 \pm 1.1 \times 10^{-2}$ cm^2 V^{-1} s^{-1}, i.e., within one standard deviation. These differences are reflected in the maximum currents measured in the transfer curves of the representative devices as well. There are also significant differences in threshold voltages between casting conditions for the transfer curves shown in Figure 5c, however overall there was a large spread in threshold voltages across all devices and no indication of significant correlation between threshold voltages and extracted mobility (see Section S9 in the Supporting Information for details). These improvements in in-plane charge mobility after annealing are consistent with our hypothesis based on the variable temperature GIWAXS measurements

that showed films with sidechain crystallinity having increased in-plane π-stacking intensity after annealing, the 2D scattering pattern of which is shown in Figure 4b.

To expand on the relationship between in-plane π-stacking and mobility in FTAZ films, the π-stacking peaks for drop-cast and spin-cast films, before and after annealing, were quantitatively analyzed. Normalized 1D ± 10° in-plane sector averages are plotted in Figure 5a, where large differences in intensity of the π-stacking peak at ≈1.68 Å^{-1} are plainly evident. Peak fits to the 1D profiles yielded peak areas which were normalized to the highest value and plotted in Figure 5b. The drop-cast and spin-cast films initially have the same in-plane π-stacking intensity (within error) but after annealing, there is a 165% increase for the drop-cast sample and a 32% decrease in the spin-cast sample. The relative π-stacking intensities of the four conditions are noticeably very similar to the average mobilities, with the exception of the average mobility of the spin-cast devices improving within the margin of error after annealing. Normalized pole figures of the π-stacking peak for each preparation condition (provided in Section S9 in the Supporting Information) show this increase in in-plane intensity as well.

For further confirmation that improved in-plane π-stacking is the cause of the improved mobility after melting for FTAZ films that exhibit sidechain crystallinity, we performed the same experiments using CB and dichlorobenzene (DCB) as solvents, characterizing the in-plane π-stacking with GIWAXS as well as the changes in OFET performance before and after annealing. A table of average device parameters and the 1D in-plane GIWAXS profiles for all three solvents, spin-cast and drop-cast, before and after annealing are shown in Section S9 (Supporting Information), as well as a table of measured film thicknesses.

We observe on average the mobility for all drop-cast devices is 2.7 times higher after annealing, with similar improvements in in-plane π-stacking intensity, while spin-cast device mobilities are only 1.4 times higher after annealing. Comparing both casting conditions after annealing for all solvents, the drop-cast devices have 2.5 times the mobility of the spin-cast.

The competition in ordering between sidechains and backbones was investigated in other SCPs with varying degree of typical alkyl stacked ($h00$) ordering and paracrystallinity, as well as stereochemistry. For this purpose, six other polymers were drop-cast from CB: poly[N-9′-heptadecanyl-2,7-carbazole-alt-5,5-(4′,7′-di-2-thienyl-2′,1′,3′-benzothiadiazole)] (PCDTBT),[57] poly{[N,N′-bis(2-octyldodecyl)-naphthalene-1,4,5,8-bis(dicarboximide)-2,6-diyl]-alt-5,5′-(2,2′-bithiophene)} (P(NDI2OD-T2)) (N2200),[58] poly(3-hexylthiophene-2,5-diyl) (P3HT), poly[(5,6-difluoro-2,1,3-benzothiadiazol-4,7-diyl)-alt-(3,3′′′-di(2-octyldodecyl)-2,2′;5′,2′′;5′′,2′′′-quaterthiophen-5,5′′′-diyl)] (PffBT4T-2OD),[59] poly{2,2′-[(2,5-bis(2-hexyldecyl)-3,6-dioxo-2,3,5,6-tetrahydropyrrolo[3,4-c]pyrrole-1,4-diyl)dithiophene]-5,5′-diyl-alt-thiophen-2,5-diyl} (PDPP3T),[60] and poly(benzodithiophene-benzotriazole) (PBnDT-HTAZ).[61] PCDTBT and PBnDT-HTAZ are both relatively amorphous for typical as-cast processing conditions, while N2200, P3HT, PffBT4T-2OD, and PDPP3T are all more crystalline in their alkyl stacking and π-stacking directions. We note that the sidechains in these materials have significant variation in length, branching, and attachment density. **Figure 6**a–c shows normal incidence TEY NEXAFS spectra of drop-cast and spin-cast films for PCDTBT, N2200, and P3HT, respectively. The spectra from the drop-cast films of all three materials exhibit the distinct double C 1s → σ^{*}_{C-H} peaks at 287.4 and 288.1 eV and, to varying degree, a decreased intensity in the C–C region at 293 eV relative to the
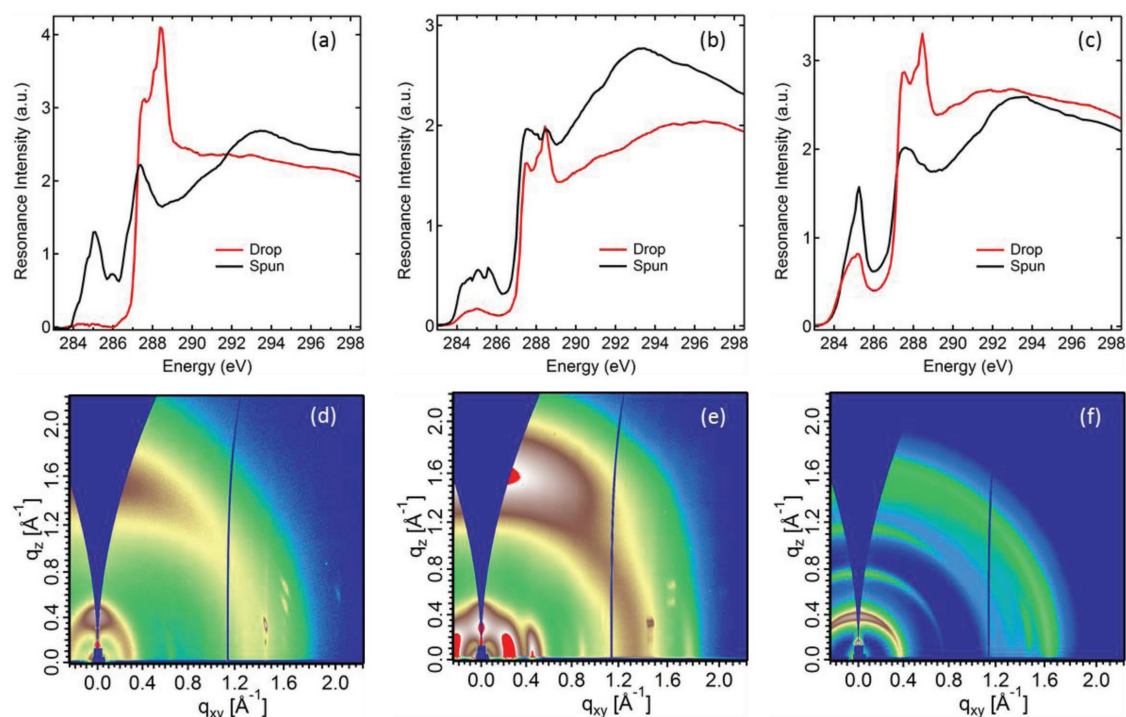

Figure 6. a–c) TEY NEXAFS spectra at normal incidence of drop-cast and spin-cast films of PCDTBT, N2200, and P3HT, respectively. d–f) 2D GIWAXS patterns from drop-cast films of PCDTBT, N2200, and P3HT, respectively.

full range of the spectra, which signify alkyl sidechain crystallinity with the alkyl chain axis oriented roughly out-of-plane for these materials as well. The GIWAXS data for the drop-cast films in Figure 6d–f also show very similar distinct, sharp features indicative of a high degree of sidechain ordering as observed for drop-cast FTAZ. GIWAXS data for the remaining three polymers are shown in Section S10 (Supporting Information). Every SCP drop-cast from CB exhibited some degree of similar sidechain GIWAXS features to those we observed for FTAZ, and NEXAFS data for PCDTBT, N2200, and P3HT films confirm sidechain crystallinity. This demonstrates that this high degree of alkyl sidechain ordering is readily achievable across SCPs with a various alkyl sidechains, typical backbone crystallinities, and monomer structures when a slow solvent quench is utilized. Importantly, the NEXAFS features of PCDTBT, N2200, and P3HT corresponding to the backbone (≈284–286 eV region), show not only greatly altered intensities between drop-cast and spin-cast samples, but also the same conspicuous broadening of the features in the drop-cast samples as observed for FTAZ and previously reported for torsionally disordered P3HT backbones.[50] This implies that the backbone ordering is also reduced in drop-cast PCDTBT, N2200, and P3HT due to backbone torsion and twisting and that the competition between ordering of the sidechains and the backbone resulting in frustrated ordering overall is a general phenomenon in SCPs with significant ramifications for molecular design, material processing, and device performance.

The fact that the strong sidechain ordering is observed for slow drying conditions that allow exploring many conformations and their energetic landscapes to lock in low energy highly ordered conformations indicates that states with crystalline sidechains are thermodynamically preferred at RT. All the materials investigated here (FTAZ, PCDTBT, N2200, P3HT, PffBT4T-2OD, PDPP3T, and PBnDT-HTAZ) are thus typically quenched by conventional processing into an unstable state when used in transistors or photovoltaics, irrespective of whether they are spin-cast and used as-is or annealed, as the annealing is typically above the melting temperature of the sidechains and the amorphous liquid structure of the sidechains is quenched into place upon cooling. This nonequilibrium state must cause problems with device stability and needs to be vitrified by either having materials with very high glass transition temperature or eliminated by engineering materials where synergistic ordering of the backbone and the sidechains are achieved in thermodynamically stable packing configurations.

We note that prior work by Kang et al. with fluorinated unbranched sidechains with the use of naphthalenediimide (NA)-based polymers is instructive in providing context and outlook.[35] The use of strongly interacting fluorinated, straight sidechains has been used to improve the backbone ordering and increase thin film transistor mobilities. Interestingly, the (001) spacing along the backbone of two different NDI-based polymers was no longer dependent on the intrinsic spacing of the repeat units in an isolated polymer chain, but driven by the spacing of the sidechain ordering. In one instance, the backbone in the order solid-state was actually stretched relative to the isolated chain. We envision that such "strain engineering" can be a general feature of SCPs, even with alkyl sidechains, if the materials are designed accordingly. The improvements observed by Kang et al. were solely attributed

to the use of highly ordering sidechains. We note though that the replacement of the typical branched sidechains of unequal length with straight sidechains is reducing the number of enantiomers. We conjecture that the usual lack of stereochemical control must also have an impact on the structure and energetic disorder of SCPs and that ordering and performance can still be greatly increased. Interestingly, the recently observed long-range exciton transport of >200 nm was observed in a material that is a single enantiomer,[62] as is IDTBT which provides "disorder free" self-assembly.[63]

3. Conclusions

In conclusion, the discovery and results presented here comprise and describe a highly ordered alkyl sidechain crystal phase in an ordered–disordered multilayer with SCP backbone layers that can form across a diverse range of SCPs, including D–A SCPs with asymmetric monomer and sidechain structures, previously considered amorphous. The sidechain coherence lengths within an ordered alkyl sidechain layer of FTAZ (in-plane in the sample) of at least 70 nm are unusually large with possibly correlated domains that might be tens of micrometers in size, as implied by optical microscopy. The ordering normal to the multilayer (generally out-of-plane) is also unusually long-range (at least 100 nm) and unambiguously correlated to the in-plane multilayer ordering, as shown by temperature-dependent diffraction measurements. The observation of multilayer formation with crystalline alkyl layers implies that the driving force for alkyl ordering is very strong. For FTAZ, N2200, P3HT, and PCDTBT, TEY NEXAFS data indicate that the highly ordered sidechain phase induces significant torsional/twisting disorder in the polymer backbone, preventing π-stacking between neighboring chains, which is supported by local UV–vis measurements in FTAZ. Our results delineate the competition in ordering between sidechains and backbones that induces the ordered/disordered multilayer microstructure or, depending on processing, layers with more ordered backbones, but disordered sidechains. This clearly implies that none of the materials investigated can be readily processed into crystals where both the sidechains and the backbone have high degrees of ordering simultaneously with all the associated diffraction peaks observable at the same time. Such competing ordering likely explains g values >6% observed for most SCPs with alkyl sidechains, and why high degrees of backbone and sidechain ordering have only been observed simultaneously in exceptional cases.[35,64]

For FTAZ, we demonstrate how the sidechain ordering–induced microstructure and subsequent melting can be used to make films with an atypical edge-on texture, which we used to improve OFET mobility by a factor of 2.5 relative to spin-cast control devices. An important implication is that the molecular packing in SCPs processed by typical casting conditions is in most cases not the thermodynamically preferred state and thus devices might not be stable.

The long-range multilayer ordering (with disordered backbone layers) could, with the aid of sufficient molecular modeling and improved molecular design, potentially be used to create true crystals with optimized long-range intra- or intermolecular

order of the SCP backbone that includes control of dihedral angles of the backbone, torsional disorder, π-stacking coherence length, or slip stack arrangements to control intra- as well as intermolecular charge transport and optoelectronic coupling. Materials that could readily develop such long-range ordering would also be highly advantageous for self-assembled monolayer or Langmuir–Blodgett applications. From a material design perspective, it might be possible to design SCPs so that both backbone and sidechain moieties would simultaneously be able to easily crystallize in their separate nanophases such that there are minimal or beneficial stresses and strains on backbone units. Even approaches akin to "strain engineering" that manipulate π-stacking distances can be envisioned, reminiscent of classic small molecule crystal engineering.[65] We envision synergic sidechain and backbone ordering, leading to SCPs with much higher degrees of molecular ordering and thus vastly improved properties and performance.

4. Experimental Section

Materials: PBnDT-FTAZ and PBnDT-HTAZ were synthesized according to literature.[66] P3HT was used as purchased from Rieke, P(NDI2OD-T2) was used as purchased from Solarmer, PCDTBT was used as purchased from 1-Material, PDPP3T was used as purchased from Solarmer, and PffBT4T-2OD was used as purchased from Cal-OS.

Film Preparation: All drop-casting was done from solutions prepared at 10 mg mL^{-1} at 80 °C, stirred 12 h. Solution was removed from the vial at 80 °C in a nitrogen-purged glovebox and immediately pipetted onto RT substrates and left to dry. For GIWAXS and NEXAFS samples, substrates were Si wafers with native oxide, for DSC, substrates were glass slides, while OFET test beds are described below. After films were visibly dry, they were placed under vacuum for at least 48 h to remove residual solvent. Spin-cast films were prepared as described previously for OFETs,[53] though for films used as control samples not in OFET measurements (i.e., GIWAXS, TEY, DSC), the annealing step prescribed for OFETs was not done, instead they were allowed to dry at RT. Blade coating (data in Section S7 in the Supporting Information) was performed in air on a heated stage at 50 °C with a glass slide used as the blade attached to a motorized track at a 4° angle relative to the sample plane. Solution was pipetted under the edge of the blade and then the track was engaged at 100 mm s^{-1}. The sample was then immediately removed from the stage.

OFET Substrate Preparation: OFET substrates were heavily doped Si (500 μm) with a conductivity of (0.2–1) × 10^3 S cm^{-1}, and a 300 nm thick layer of SiO$_2$ as the gate dielectric. To fabricate the transistor test beds, Ti (10 nm)/Au (40 nm) contacts were evaporated on prepatterned substrates. Test beds were cleaned, UVO$_3$ treated, and octadecyltrichlorosilane self-assembled monolayer treated similarly to previous recipes.[53]

OFET I–V Characterization: OFETs were characterized with a Keithley 4200 Semiconductor Parameter Analyzer. The parameter analyzer was coupled with triaxial feedthroughs with a Janis probe station, where the test samples were placed in a turbo-pumped high vacuum chamber (10^{-5} mbar). For each FTAZ film condition, at least 30 devices were tested and relevant parameters extracted from slopes to transfer curves in the saturation regime. Mobilities versus V_g plots were checked for each device, as in Figure S16b (Supporting Information) to ensure the mobility was not artificially increased.

GIWAXS: GIWAXS patterns were measured at beamline 7.3.3 at the ALS with 10 keV X-rays with a Dectris Pilatus photon counting detector and a partially Helium purged scattering environment and beamline 11-3 at the SSRL with 12.7 keV X-rays, a MAR 225 charge-coupled device detector, and a completely helium-purged scattering environment.[67] After alignment, scattering patterns were recorded at well below, just

above, and well above the critical angle as determined by scattering intensity versus incident angle scans. Unless otherwise specified, the data shown corresponded to the pattern recorded just above the critical angle. The temperature dependent GIWAXS was performed using an in situ heating stage at the ALS. GIWAXS analysis was done in Igor Pro using a modified version of the NIKA software package.[68]

DSC: DSC thermograms were collected with the heating rate of 10 °C min^{-1} by TA Instruments Dicovery Series. Baseline and temperature were calibrated with sapphire and indium.

TEY NEXAFS: TEY NEXAFS spectra were measured at the soft X-ray beamline at the Australian Synchrotron.[69] Linearly polarized X-rays with $E/\Delta E \approx 10\,000$ were focused to an ≈0.4 mm × 1 mm spot. Samples were measured under ultrahigh vacuum. The TEY signal was recorded via the drain current through the sample. Analysis of spectra is described in Section S2 (Supporting Information).

Micro-UV–vis: Micro-UV–vis spectra were obtained with a CRAIC Technologies 20/30 PV Microspectrophotometer. A Xe lamp was chosen as the light source illuminating the sample. Samples were measured in transmission mode, with light collected through a Zeiss EC Epiplan Neofluar 100× objective (0.9 numerical aperture). Spectra were measured over a 1.21 μm^2 area using a built-in aperture, with a 10 s collection time and 10 spectral averaging in the range of 350–800 nm.

Supporting Information

Supporting Information is available from the Wiley Online Library or from the author.

Conflict of Interest

The authors declare no conflict of interest.

Keywords

molecular design, organic electronics, polymer crystals, semiconducting polymers, sidechains

[1] R. X. Xie, Y. Lee, M. P. Aplan, N. J. Caggiano, C. Muller, R. H. Colby, E. D. Gomez, *Macromolecules* **2017**, *50*, 5146.
[2] F. P. V. Koch, M. Heeney, P. Smith, *J. Am. Chem. Soc.* **2013**, *135*, 13699.
[3] Y. Yuan, J. M. Zhang, J. Q. Sun, J. Hu, T. P. Zhang, Y. X. Duan, *Macromolecules* **2011**, *44*, 9341.
[4] Y. Yuan, J. M. Zhang, J. Q. Sun, *Macromolecules* **2011**, *44*, 6128.
[5] S. Pankaj, M. Beiner, *J. Phys. Chem. B* **2010**, *114*, 15459.
[6] S. Pankaj, M. Beiner, *AIP Conf. Proc.* **2010**, *1255*, 107.
[7] P. Arosio, M. Moreno, A. Famulari, G. Raos, M. Catellani, S. V. Meille, *Chem. Mater.* **2009**, *21*, 78.
[8] Y. Guo, L. Wang, Y. Y. Han, Y. H. Geng, Z. H. Su, *Polym. Chem.* **2014**, *5*, 1938.
[9] L. Brambilla, M. Tommasini, I. Botiz, K. Rahimi, J. O. Agumba, N. Stingelin, G. Zerbi, *Macromolecules* **2014**, *47*, 6730.
[10] R. Remy, S. Wei, L. M. Campos, M. E. Mackay, *ACS Macro Lett.* **2015**, *4*, 1051.
[11] F. Panzer, M. Sommer, H. Bassler, M. Thelakkat, A. Kohler, *Macromolecules* **2015**, *48*, 1543.
[12] F. Panzer, H. Bassler, A. Kohler, *J. Phys. Chem. Lett.* **2017**, *8*, 114.
[13] R. Noriega, J. Rivnay, K. Vandewal, F. P. V. Koch, N. Stingelin, P. Smith, M. F. Toney, A. Salleo, *Nat. Mater.* **2013**, *12*, 1038.
[14] D. M. DeLongchamp, R. J. Kline, Y. Jung, E. K. Lin, D. A. Fischer, D. J. Gundlach, S. K. Cotts, A. J. Moad, L. J. Richter, M. F. Toney, M. Heeney, I. McCulloch, *Macromolecules* **2008**, *41*, 5709.
[15] T. Babur, G. Gupta, M. Beiner, *Soft Matter* **2016**, *12*, 8093.
[16] S. Pankaj, E. Hempel, M. Beiner, *Macromolecules* **2009**, *42*, 716.
[17] F. C. Spano, *J. Chem. Phys.* **2005**, *122*, 234701.
[18] J. Clark, J. F. Chang, F. C. Spano, R. H. Friend, C. Silva, *Appl. Phys. Lett.* **2009**, *94*, 163306.
[19] A. Salleo, R. J. Kline, D. M. DeLongchamp, M. L. Chabinyc, *Adv. Mater.* **2010**, *22*, 3812.
[20] I. McCulloch, M. Heeney, C. Bailey, K. Genevicius, I. Macdonald, M. Shkunov, D. Sparrowe, S. Tierney, R. Wagner, W. Zhang, M. L. Chabinyc, R. J. Kline, M. D. McGehee, M. F. Toney, *Nat. Mater.* **2006**, *5*, 328.
[21] H. Sirringhaus, P. J. Brown, R. H. Friend, M. M. Nielsen, K. Bechgaard, B. M. W. Langeveld-Voss, A. J. H. Spiering, R. A. J. Janssen, E. W. Meijer, P. Herwig, D. M. de Leeuw, *Nature* **1999**, *401*, 685.
[22] J. Rivnay, M. F. Toney, Y. Zheng, I. V. Kauvar, Z. H. Chen, V. Wagner, A. Facchetti, A. Salleo, *Adv. Mater.* **2010**, *22*, 4359.
[23] G. Kim, S. J. Kang, G. K. Dutta, Y. K. Han, T. J. Shin, Y. Y. Noh, C. Yang, *J. Am. Chem. Soc.* **2014**, *136*, 9477.
[24] S. Chen, H. J. Cho, J. Lee, Y. K. Yang, Z. G. Zhang, Y. F. Li, C. Yang, *Adv. Energy Mater.* **2017**, *7*, 1701125.
[25] H. Sirringhaus, N. Tessler, R. H. Friend, *Science* **1998**, *280*, 1741.
[26] X. B. Shen, V. V. Duzhko, T. P. Russell, *Adv. Energy Mater.* **2013**, *3*, 263.
[27] R. Mauer, M. Kastler, F. Laquai, *Adv. Funct. Mater.* **2010**, *20*, 2085.
[28] W. M. Zhang, J. Smith, S. E. Watkins, R. Gysel, M. McGehee, A. Salleo, J. Kirkpatrick, S. Ashraf, T. Anthopoulos, M. Heeney, I. McCulloch, *J. Am. Chem. Soc.* **2010**, *132*, 11437.
[29] J. Y. Liu, R. Zhang, G. Sauve, T. Kowalewski, R. D. McCullough, *J. Am. Chem. Soc.* **2008**, *130*, 13167.
[30] X. Leng, H. B. Yin, D. M. Liang, Y. C. Ma, *J. Chem. Phys.* **2015**, *143*, 114501.
[31] G. Horowitz, B. Bachet, A. Yassar, P. Lang, F. Demanze, J. L. Fave, F. Garnier, *Chem. Mater.* **1995**, *7*, 1337.
[32] O. Alexiadis, V. G. Mavrantzas, *Macromolecules* **2013**, *46*, 2450.
[33] M. Bockmann, T. Schemme, D. H. de Jong, C. Denz, A. Heuer, N. L. Doltsinis, *Phys. Chem. Chem. Phys.* **2015**, *17*, 28616.
[34] Y. K. Lan, C. I. Huang, *J. Phys. Chem. B* **2009**, *113*, 14555.
[35] B. Kang, R. Kim, S. B. Lee, S. K. Kwon, Y. H. Kim, K. Cho, *J. Am. Chem. Soc.* **2016**, *138*, 3679.
[36] J. Stöhr, *NEXAFS Spectroscopy*, Springer-Verlag, Berlin **1992**.
[37] J. Stohr, D. A. Outka, K. Baberschke, D. Arvanitis, J. A. Horsley, *Phys. Rev. B* **1987**, *36*, 2976.
[38] A. P. Hitchcock, I. Ishii, *J. Electron Spectrosc. Relat. Phenom.* **1987**, *42*, 11.
[39] R. D. Peters, P. F. Nealey, J. N. Crain, F. J. Himpsel, *Langmuir* **2002**, *18*, 1250.
[40] A. Scholl, R. Fink, E. Umbach, G. E. Mitchell, S. G. Urquhart, H. Ade, *Chem. Phys. Lett.* **2003**, *370*, 834.
[41] K. Weiss, H. Ostrom, L. Triguero, H. Ogasawara, M. G. Garnier, L. G. M. Pettersson, A. Nilsson, *J. Electron Spectrosc. Relat. Phenom.* **2003**, *128*, 179.
[42] G. Hahner, M. Kinzler, C. Woll, M. Grunze, M. K. Scheller, L. S. Cederbaum, *Phys. Rev. Lett.* **1991**, *67*, 851.
[43] S. Swaraj, H. Ade, *J. Electron Spectrosc. Relat. Phenom.* **2013**, *191*, 60.
[44] J. R. Tumbleston, A. C. Stuart, E. Gann, W. You, H. Ade, *Adv. Funct. Mater.* **2013**, *23*, 3463.
[45] A. P. Hitchcock, J. A. Horsley, J. Stohr, *J. Chem. Phys.* **1986**, *85*, 4835.
[46] B. Watts, S. Swaraj, D. Nordlund, J. Lüning, H. Ade, *J. Chem. Phys.* **2011**, *134*, 024702.
[47] S. G. Urquhart, A. P. Smith, H. W. Ade, A. P. Hitchcock, E. G. Rightor, W. Lidy, *J. Phys. Chem. B* **1999**, *103*, 4603.
[48] S. G. Urquhart, H. Ade, *J. Phys. Chem. B* **2002**, *106*, 8531.
[49] O. Dhez, H. Ade, S. G. Urquhart, *J. Electron Spectrosc. Relat. Phenom.* **2003**, *128*, 85.
[50] S. G. Urquhart, M. Martinson, S. Eger, V. Murcia, H. Ade, B. A. Collins, *J. Phys. Chem. C* **2017**, *121*, 21720.
[51] N. Norman, H. Mathisen, *Acta Chem. Scand.* **1972**, *26*, 3913.
[52] R. Boese, H. C. Weiss, D. Blaser, *Angew. Chem., Int. Ed.* **1999**, *38*, 988.
[53] B. H. Smith, Q. Q. Zhang, M. A. Kelly, J. H. Litofsky, D. Kumar, A. Hexemer, W. You, E. D. Gomez, *ACS Macro Lett.* **2017**, *6*, 1162.
[54] S. W. Lee, H. S. Keum, H. S. Kim, H. J. Kim, K. Ahn, D. R. Lee, J. H. Kim, H. H. Lee, *Macromol. Rapid Commun.* **2016**, *37*, 203.
[55] W. E. Acree, *Thermochim. Acta* **1991**, *189*, 37.
[56] U. Domanska, D. Wyrzykowskastankiewicz, *Thermochim. Acta* **1991**, *179*, 265.
[57] N. Blouin, A. Michaud, M. Leclerc, *Adv. Mater.* **2007**, *19*, 2295.
[58] H. Yan, Z. Chen, Y. Zheng, C. Newman, J. R. Quinn, F. Dotz, M. Kastler, A. Facchetti, *Nature* **2009**, *457*, 679.
[59] Y. Liu, J. Zhao, Z. Li, C. Mu, W. Ma, H. Hu, K. Jiang, H. Lin, H. Ade, H. Yan, *Nat. Commun.* **2014**, *5*, 5293.

**ADVANCED
SCIENCE NEWS**

www.advancedsciencenews.com

**ADVANCED
FUNCTIONAL
MATERIALS**

www.afm-journal.de

[60] J. C. Bijleveld, A. P. Zoombelt, S. G. J. Mathijssen, M. M. Wienk, M. Turbiez, D. M. de Leeuw, R. A. J. Janssen, *J. Am. Chem. Soc.* **2009**, *131*, 16616.

[61] S. C. Price, A. C. Stuart, L. Yang, H. Zhou, W. You, *J. Am. Chem. Soc.* **2011**, *133*, 4625.

[62] X. H. Jin, M. B. Price, J. R. Finnegan, C. E. Boott, J. M. Richter, A. Rao, M. Menke, R. H. Friend, G. R. Whittell, I. Manners, *Science* **2018**, *360*, 897.

[63] D. Venkateshvaran, M. Nikolka, A. Sadhanala, V. Lemaur, M. Zelazny, M. Kepa, M. Hurhangee, A. J. Kronemeijer, V. Pecunia, I. Nasrallah, I. Romanov, K. Broch, I. McCulloch, D. Emin, Y. Olivier, J. Cornil, D. Beljonne, H. Sirringhaus, *Nature* **2014**, *515*, 384.

[64] Y. Yuan, J. Shu, P. Liu, Y. P. Zhang, Y. X. Duan, J. M. Zhang, *J. Phys. Chem. B* **2015**, *119*, 8446.

[65] G. Giri, E. Verploegen, S. C. B. Mannsfeld, S. Atahan-Evrenk, D. H. Kim, S. Y. Lee, H. A. Becerril, A. Aspuru-Guzik, M. F. Toney, Z. A. Bao, *Nature* **2011**, *480*, 504.

[66] Q. Q. Zhang, L. Yan, X. C. Jiao, Z. X. Peng, S. B. Liu, J. J. Rech, E. Klump, H. Ade, F. So, W. You, *Chem. Mater.* **2017**, *29*, 5990.

[67] A. Hexemer, W. Bras, J. Glossinger, E. Schaible, E. Gann, R. Kirian, A. MacDowell, M. Church, B. Rude, H. Padmore, *J. Phys.: Conf. Ser.* **2010**, *247*, 012007.

[68] J. Ilavsky, *J. Appl. Crystallogr.* **2012**, *45*, 324.

[69] B. C. C. Cowie, A. Tadich, L. Thomsen, *AIP Conf. Proc.* **2010**, *1234*, 307.

1806977 (13 of 13)